



# Simulation of Concrete Plate Perforation by Coupled Finite Element and Smooth Particle Hydrodynamics Methods

Dmitriev, A.<sup>1\*</sup>; Lalin, V.<sup>1</sup>; Novozhilov, Yu.<sup>2</sup>; Mikhalyuk, D.<sup>3</sup>

<sup>1</sup> Peter the Great St. Petersburg Polytechnic University, St. Petersburg, Russian Federation

<sup>2</sup> CADFEM CIS, JSC, St. Petersburg, Russian Federation

<sup>3</sup> Center of Engineering Physics, Simulation and Analysis, JSC, St. Petersburg, Russian Federation

\* [dmitriefan@outlook.com](mailto:dmitriefan@outlook.com)

## Keywords:

Concretes; Calibration; Computer simulation; Ballistics; Constitutive models; Strength; Numerical models; Finite element method; Smoothed Particle Hydrodynamics

## Abstract:

**The object of research** is a concrete plate subjected to high-velocity projectile impact. The finite element method (FEM) is commonly used to obtain the nonlinear dynamic response of concrete structures. However, extreme loads such as projectile impact cause large strains, damages, material fragmentations. The mesh-based FEM cannot solve this task accurately. Smoothed particle hydrodynamics (SPH) is the meshless method that allows us to solve perforation and fragmentation problems but is characterized by higher computational costs. **Methods.** In this paper, we use the coupled FEM-SPH method to simulate the high-velocity concrete plate perforation. This method derives from switching from FEM to SPH by specific triggering criterion. Shear strain is the triggering criterion for the concrete plate perforation problem. The elastoplastic-damage Continuous Cap Surface Model (CSCM) describes nonlinear stress-strain relationships with strain-rate dependency for concrete. **Results.** Validation of CSCM on quasi-static cube compression gives good agreement with Eurocode-2 data: difference does not exceed 7% in FEM and 3.8% in the SPH method, respectively. For concrete plate perforation, the best match with the experiment is for the numerical model with spacings between FE nodes, and between SPH particles are equal to 2 mm. In this case, the ratio between the projectile diameter and the spatial discretization of approximately 6:1. The triggering value of shear strain for switching from FEM to SPH seems not to influence modeling results and computing time, independently of spatial discretization.

## 1 Introduction

Concrete is a frequently used material subjected to static and intense dynamic loadings in civil and defense engineering. In contrast to static loads [1], most extreme loads such as projectile impact, blast, earthquakes have a highly nonlinear dynamic nature and often lead to large deformations and damages in RC structures.

Mainly, the finite element method (FEM) based on Lagrange formulation [2]–[9] is used to calculate the nonlinear response of concrete structures under extreme loads [10]–[12]. However, significant distortion of a finite element can cause a negative Jacobian determinant, which can lead to negative element volume and unexpected termination of the FEM computations [13], [14]. Moreover, FEM cannot describe changes in structure topology and, therefore, cannot solve perforation problems.

Element erosion technique is often used to overcome problems related to mesh distortion. This approach implies that the distorted elements are removed from the numerical model once a user-specified failure criterion is met. In the context of concrete structures simulation, the failure criterion usually is a strain-based limit or damage value. However, the element erosion technique has some serious shortcomings: strong mesh-size dependency, exclusion of damaged concrete from the contact interaction with other objects, and loss of mass and momentum in the system. All this leads to incorrect results and limits the use of element erosion [13], [15].

An alternative approach is to use the meshfree method, which is naturally suitable for high deformation, large strain, and material fragmentation. The most popular meshfree method is the smooth particle hydrodynamics (SPH) method developed by Lucy, Gingold, Monaghan for astrophysics problems [16]–[20] and then adopted as one of the efficient computational techniques to solve applied mechanics problems [15], [21]–[23]. The disadvantage of the SPH method in comparison with FEM is the high computational cost [14], [24].

The SPH method can be used for structural response calculation only in a zone where extreme distortions are expected to reduce computational demand; meanwhile, FEM is used in regions with lower distortions. Therefore, coupling SPH and FEM seems a reasonable approach to take advantage of both methods, which can provide a tool capable of modeling the interaction of bodies subjected to large deformation [25].

Despite the presence of many works related to the application of the coupled FEM-SPH method in modeling the structural dynamic response [14], [15], [24], [26], there are no studies on the choice of spatial discretization and FEM-SPH triggering criterion for an effective and accurate solution in modeling the projectile impact on concrete structures.

Thus, the main aim of this study is to validate the coupled FEM-SPH method for projectile impact simulations of concrete structures. The study objectives are:

1. Validation the concrete constitutive model both by FEM and SPH in quasi-static cube compression;
2. Influence of different spatial discretization in projectile impact simulation;
3. Robustness to a varying value of purposed FEM-SPH triggering criterion;
4. Computational costs in different problem setup cases estimation and comparison.

## 2 Materials and Methods

The problem of high-velocity projectile impact on the concrete plate is considered, experimental results can be found in [27]. It is known that the steel projectile with the initial velocity of 749 m/s hits the concrete slab, perforates it, and continues to move with a residual velocity equal to 615 m/s. Details of the experiment are shown in Figure 2.1.

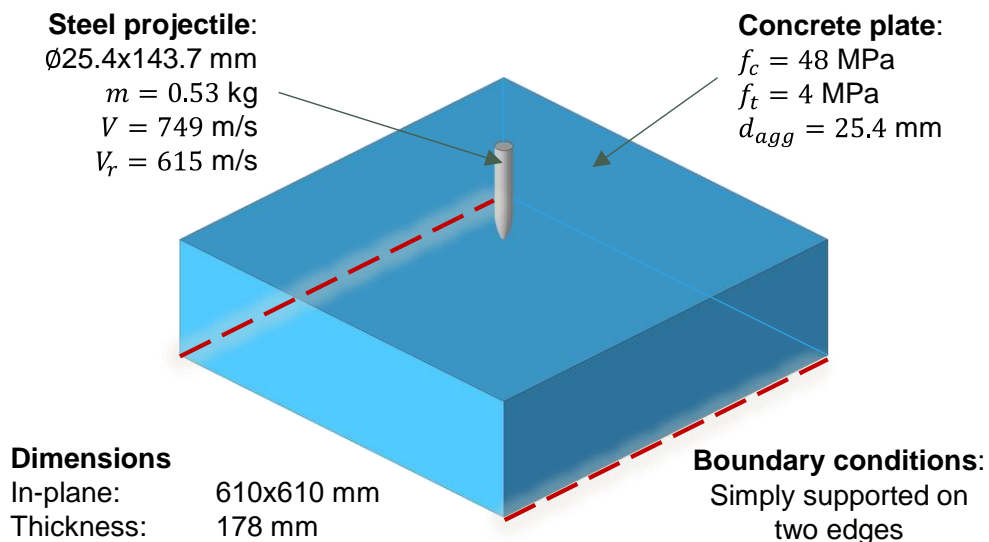


**Figure 2.1 – Problem description**

Numerical simulations in this study are conducted by LS-DYNA software [28]. For all simulations, a workstation with Intel Core i7-7700K CPU (4 cores, 4.20 GHz) and 32 GB RAM is used. Simulations are performed by LS-DYNA R10.1.0 version with double precision solver and shared memory parallel computing.

The main idea is to combine the advantages of both FEM and SPH method [14], [15], [24], [26]. Initially, the projectile impact is simulated by FEM. The concrete plate is discretized by quadratic fully integrated 8-node hexahedrons with nodal rotations (ELFORM=3 in \*SECTION\_SOLID keyword). At simulation starts, one or more inactive SPH particles (depends on the NQ parameter in

\*DEFINE\_ADAPTIVE\_SOLID\_TO\_SPH keyword) are created inside the volume of each FE in the central part subjected to projectile impact as shown in Figures 2.3–2.3.

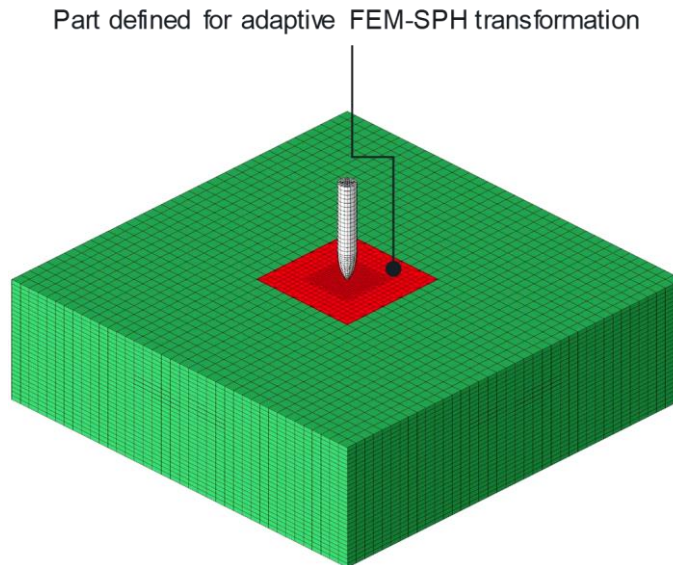


Figure 2.2 – Concrete plate area defined for adaptive FEM-SPH transformation

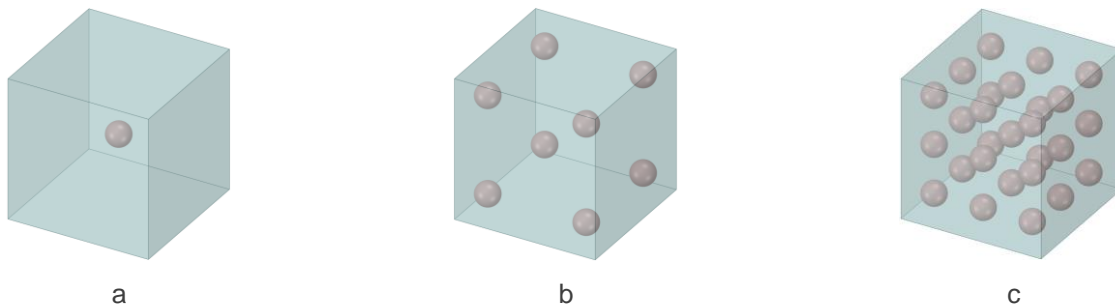


Figure 2.3 – Particles density after adaptive transforming from finite element: a – low (NQ=1: 1 FE → 1 SPH particle); a – medium (NQ=2: 1 FE → 8 SPH particles); c – high (NQ=3: 1 FE → 27 SPH particles)

These SPH particles are inactive until the triggering criterion meets. In this paper, shear strain is used as a triggering criterion, and its value is studied in the next section from the position of the best agreement with the experimental results. When shear strain in a solid Lagrangian element reaches a predefined value (EPSSH parameter in \*MAT\_ADD\_EROSION keyword), this finite element is deleted and replaced by one or more activated SPH particles. The SPH particles replacing the failed solid Lagrangian elements inherit all the Lagrange nodal quantities and all the Lagrange integration point quantities of these failed solid elements [28]. The newly generated SPH elements are coupled to the adjacent uneroded solid elements. Details of the FEM-SPH coupling algorithm can be found in [14], [25], [29], [30].

In accordance with the SPH method foundations [22], [23], the continuum is replaced by a finite number of particles with its own physical quantities defined by the kernel function  $W(x, h)$  in support domain  $\Omega$  (see Figure 2.4). In the present simulations, cubic spline smoothing kernel function is used (SPHKERN=0 in \*SECTION\_SPH keyword):

$$W(q, h) = \frac{1}{h} \frac{1}{\pi} \begin{cases} 1 - \frac{3}{2}q^2 + \frac{3}{4}q^3 \text{ for } |q| \leq 1 \\ \frac{1}{4}(2 - q)^3 \text{ for } 1 \leq q \leq 2 \\ 0 \text{ for } 2 < |q| \end{cases} \quad (2.1)$$

where  $q = r_{ij}/h$ ,  $h$  is smoothing length.

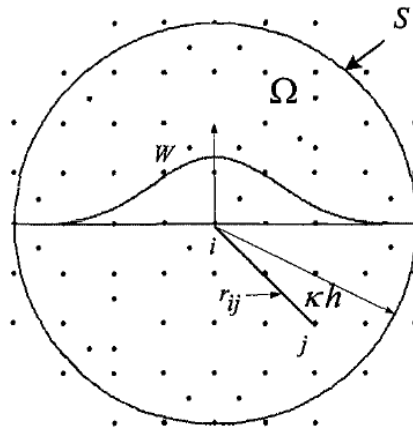


**Figure 2.4 – The support domain  $\Omega$  of the smoothing kernel  $W$  for particle  $i$**

According to expression (2.1), when the distance between two particles exceeds two smoothing lengths, these particles do not interact.

Complex interactions between steel projectile, concrete Lagrangian elements, and SPH particles are described via three \*CONTACT keywords. Since solid Lagrangian elements are deleted during the simulation, its interaction with the steel projectile and SPH particles are defined by \*CONTACT\_ERODING\_NODES\_TO\_SURFACE keywords. Contact between projectile and SPH particles is provided via \*CONTACT\_AUTOMATIC\_NODES\_TO\_SURFACE keyword. The static friction coefficient between concrete elements is 0.60 and dynamic friction coefficient is 0.35; coefficients for steel-concrete pair are equal to 0.45 and 0.20, respectively [15], [26], [31].

The choice of appropriate constitutive models for materials plays a key role in nonlinear dynamic simulations. The steel projectile and modeled as a rigid body since no erosion and deformation of the projectile was observed after the experiment [27]. Stress-strain relationships for concrete are described by Continuous Surface Cap Model (\*MAT\_CSCM keyword) [32], [33]. This elastoplastic-damage model with rate effects has been widely used for simulation of the static and dynamic response of concrete structures [10], [33]–[37].

Nonlinear behavior is described in terms of plastic flow theory by strain rate-dependent smooth yield surface  $F(I_1, J_2, J_3)$  consist of shear surface and cap surface (see Figure 2.5).

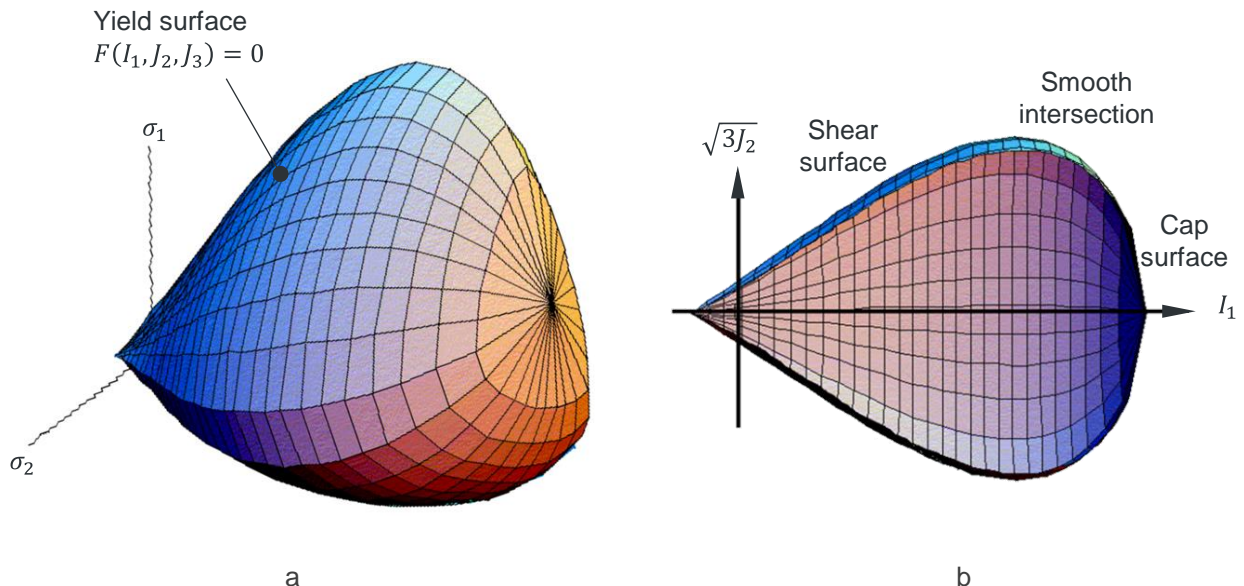


**Figure 2.5 – Yield surface in principal stress space: a – in three dimensions; b – in the meridional plane**

Constitutive relations include damage formulation and the damage parameter  $d$  to model both strength and stiffness reduction (see Figure 2.6):

$$\sigma_{ij}^d = (1 - d)\sigma_{ij} \tag{2.2}$$

$$E_{ij}^d = (1 - d)E_{ij} \tag{2.3}$$

where  $\sigma_{ij}$  and  $E_{ij}$  are undamaged stress component and undamaged elastic modulus, respectively;  $\sigma_{ij}^d$  and  $E_{ij}^d$  are its damaged values, respectively.

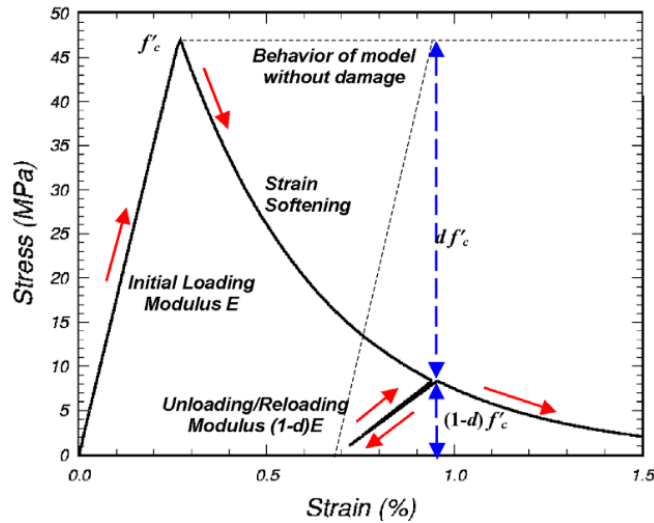


**Figure 2.6 – Strength and stiffness degradation in concrete**

Calibration of the model parameters has been performed based on the original report [32] and the article [38].

### 3 Results and discussion

#### 3.1 Concrete constitutive model validation

To validate the calibrated parameters both by FEM and SPH method against the Eurocode-2 data [39] the quasi-static compression problem of concrete cube is considered (see Figure 3.1). Cube with edge length equal to 150 mm is compressed via upper steel plates moved with the vertical velocity of 0.15 mm/s, and bottom steel plates are fixed. Interactions between plates and concrete specimen are defined by frictional contact, as described above. Distances between nodes in the FE model and particles in the SPH model are equal to 5 mm.

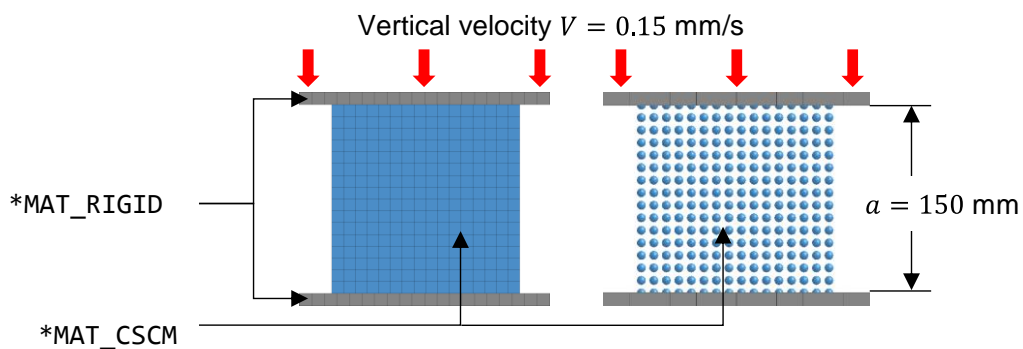


**Figure 3.1 – FE and SPH numerical models of concrete cube compression**

Four concrete grades are considered to validate the ability of the concrete material model to reproduce cube strength objectively and results are evaluated against Eurocode-2 data [39] (see Table 3.1). Typical damage distribution across the vertical central plane is shown in Figure 3.2. Stress-strain diagrams are shown in Figure 3.3. The parameters of the \*MAT\_CSCM for different concrete grades are presented in Annex A.

Table 3.1 – Cube strength for different concrete grades

Concrete grade	Cube strength according to Eurocode [MPa]	FEM		SPH	
		Value [MPa]	Error [%]	Value [MPa]	Error [%]
C20/25	25	24.0	4.0	25.0	0.0
C30/37	37	35.9	3.1	37.3	0.8
C40/50	50	46.5	7.0	48.2	3.6
C50/60	60	56.8	5.3	58.6	2.3

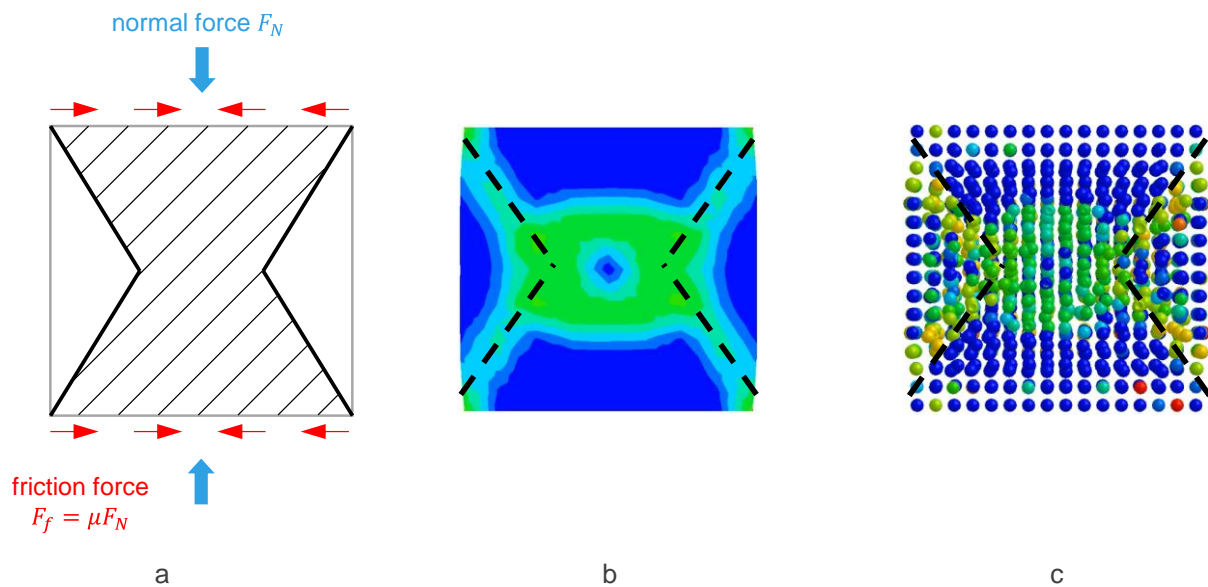
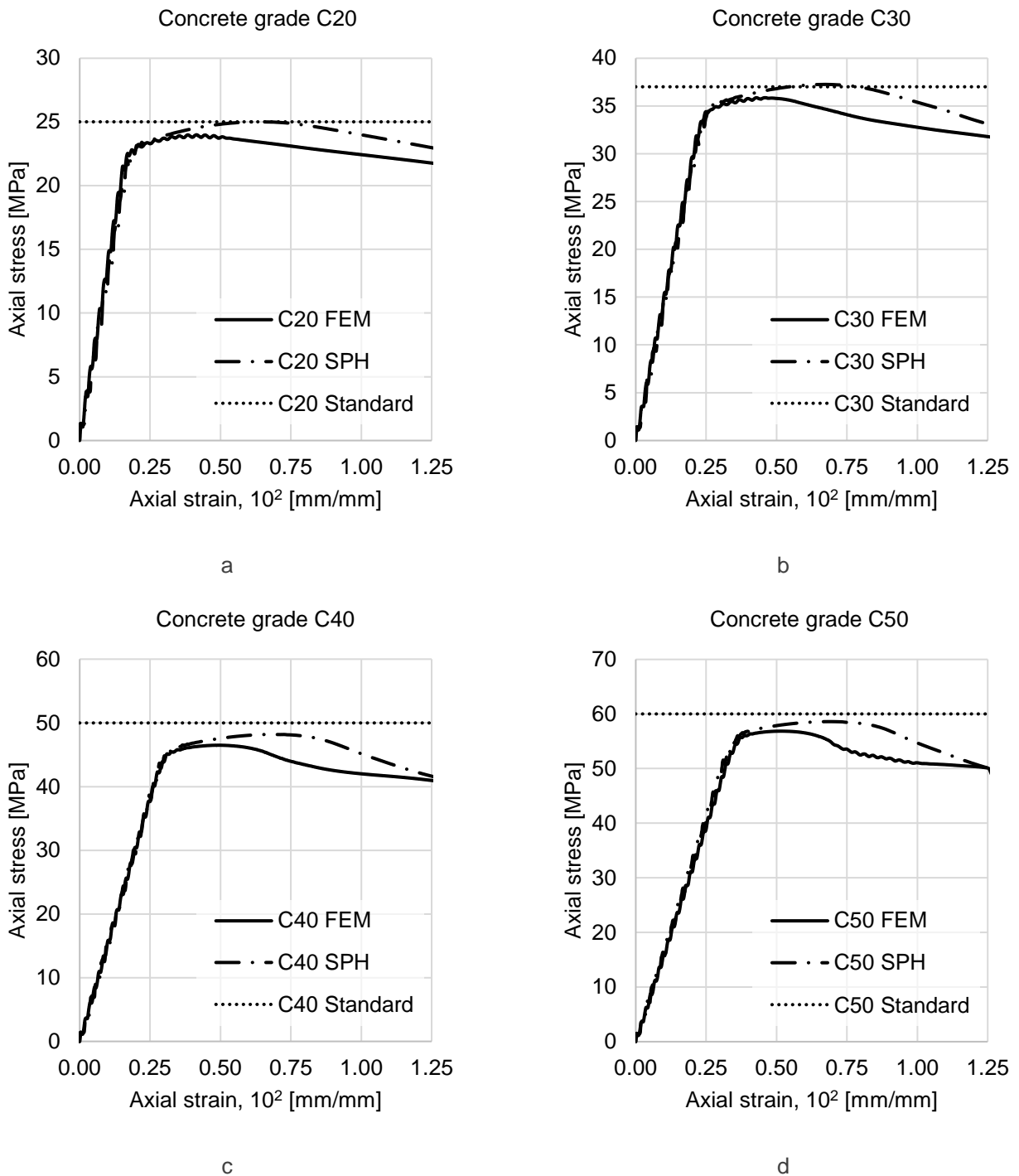


Figure 3.2 – Damage parameter distribution vertical central plane:  
a – failure mode from lab tests; b – FEM simulation; c – SPH simulation



**Figure 3.3 – Cube compression results for different concrete grades: a – C20; b – C30; c – C40; d – C50**

Damage fields presented in Figure 3.2b,c are identical both in FEM and SPH method simulations and correctly describes usual failure mode from lab tests [40] (see Figure 3.2a). Due to friction, four vertical faces break down, leaving two truncated pyramids, one inverted over the other. As presented in Table 3.1 and Figure 3.3, strength values and stress-strain relationships calculated by two methods are similar for a wide range of concrete grades. Thus, FEM and SPH calculations using the CSCM concrete model give identical results for different concrete grades and agree with the standard data [39] well.

### 3.2 High-velocity projectile impact on the concrete plate

#### 3.2.1 Description of the numerical model

The numerical model is configured for computations by the FEM-SPH method, as described in the previous section. Simulation is conducted with three mesh sizes: coarse, medium, and fine. Details of numerical models are presented in Figure 3.4 and in Table 3.2.

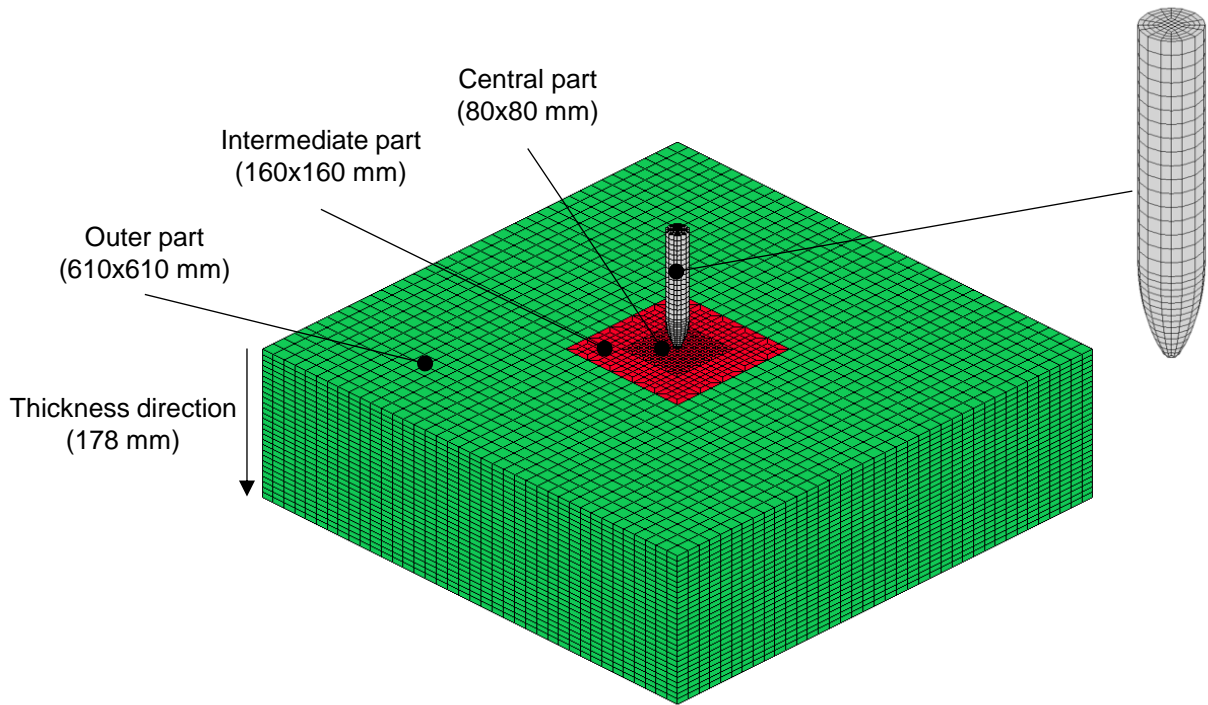


Figure 3.4 – Details of the numerical model

Table 3.2 – Finite element mesh parameters for concrete plate

Numerical model		Coarse	Medium	Fine
Element size	Thickness direction	6.4 mm	4.7 mm	3.2 mm
	Central part	4.0 mm	3.0 mm	2.0 mm
	Intermediate part	8.0 mm	6.0 mm	4.0 mm
	Outer part	16.0 mm	12.0 mm	8.0 mm
Number of elements		55 216	183 008	441 728
Number of nodes		59 421	191 919	458 337

### 3.2.2 Coupled FEM-SPH simulation

#### 3.2.2.1 Mesh size influence

During the projectile impact, the concrete slab gets damaged, as shown in Figure 3.5. Perforation of the slab leads to significant distortion of the finite element mesh and transition to the SPH particles.

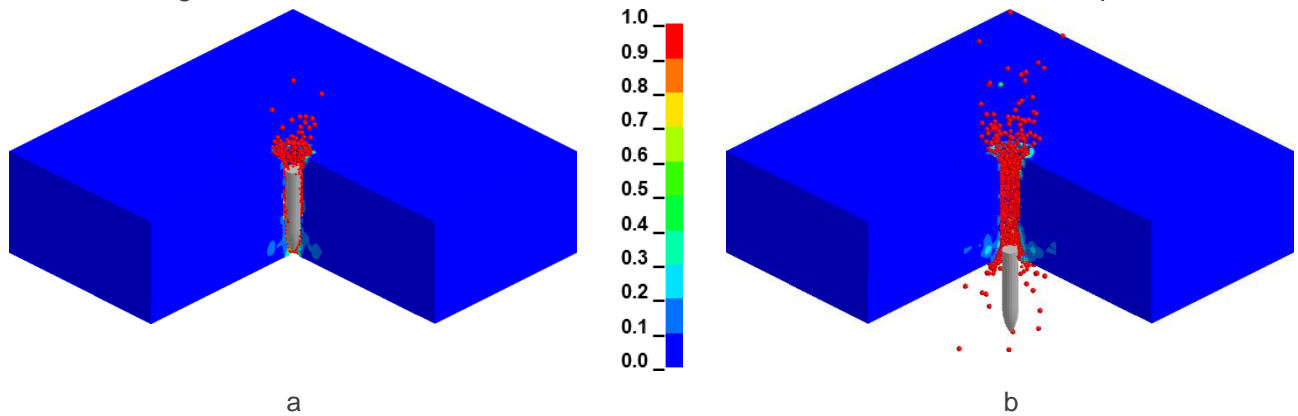


**Figure 3.5 – Damage in concrete plate:**  
**a – projectile perforates the concrete plate (260  $\mu$ s); b – projectile out of the plate (480  $\mu$ s)**

The modeling results are compared with the experimental residual velocity in Figure 3.6. Simulation errors, used RAM and requested computing time for three mesh sizes are presented in Table 3.3.

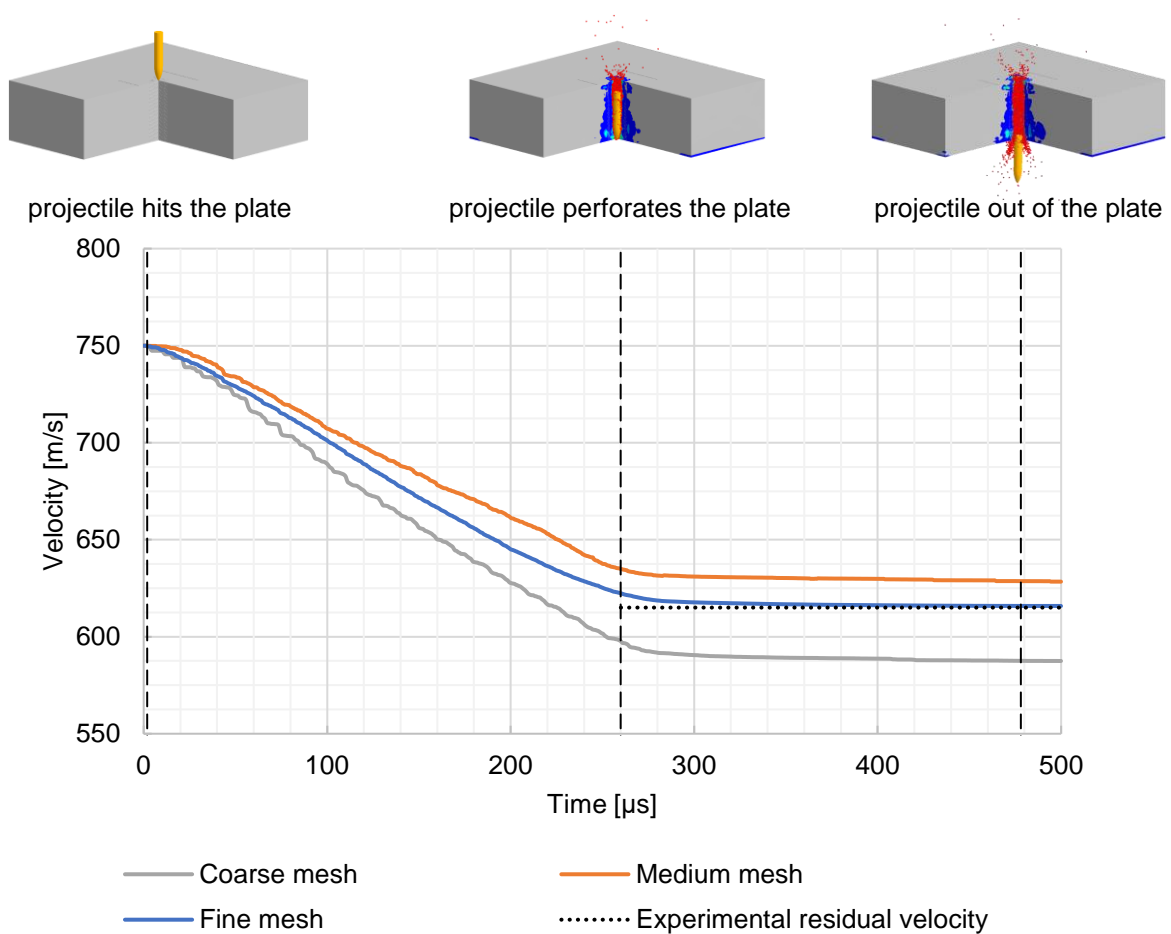


**Figure 3.6 – Projectile velocity corresponding to different FE mesh sizes**

**Table 3.3 – Simulation results and requested computational resources**

	Coarse mesh	Medium mesh	Fine mesh
Mesh size (distance between particles) [mm]	4.0	3.0	2.0
Residual velocity [m/s]	587.43	628.34	616.08
Error [%]	4.48	2.17	0.18
Used RAM [MB]	481	1915	3838
Computing time [hh:mm:ss]	00:11:07	02:35:07	04:24:54

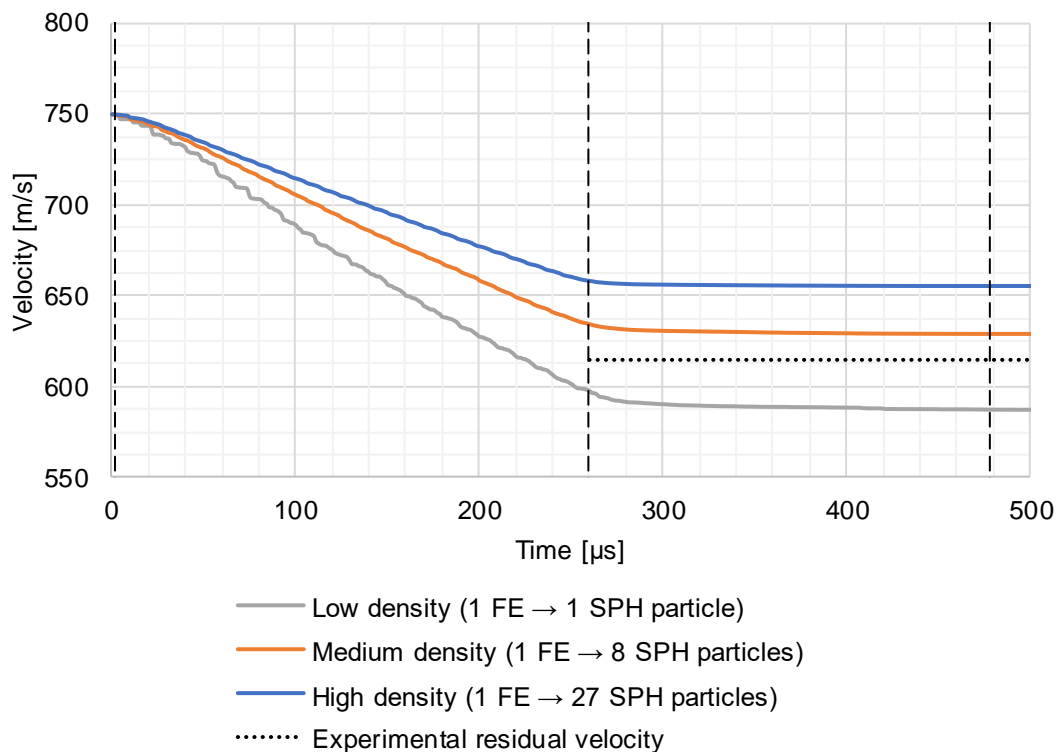
As shown in Figure 3.6 and Table 3.3, the most accurate results are obtained on model with mesh size (distance between SPH particles) is equal to 2 mm, although the most inaccurate calculation on a coarse mesh leads to an error of only 4.5%. For the numerical model with fine mesh, the ratio of the projectile diameter to the FE size is approximately 6:1.

At the same time, a finer spatial discretization leads to a dramatic change in the used RAM and computing time. A decrease of the minimum mesh size from 4 mm to 2 mm leads to an eight times increase of used RAM (from 481 MB to 3838 MB) and to 24 times increase of computing time (from 11 minutes to 4 hours 25 minutes).

### 3.2.2.2 Various densities of the SPH particles

In LS-DYNA, it is possible to set the number of SPH particles that will be activated after the FEM-SPH triggering criterion will be achieved. In this paper, three cases with  $1^3 = 1$ ,  $2^3 = 8$  и  $3^3 = 27$  particles are investigated, as shown in Figure 2.3. The simulation is conducted on a coarse mesh model. In-plane distance between SPH particles in the first case is equal to 4 mm, in the second, is 2 mm, and in the third is 1.4 mm.

Simulation results and requested computational resources are presented in Figure 3.7 and in Table 3.4.

**Figure 3.7 – Projectile velocity corresponding to different particle densities**

**Table 3.4 – Simulation results and requested computational resources for different densities of the particles**

	Low density	Medium density	High density
Distance between particles [mm]	4.0	2.0	1.4
Residual velocity [m/s]	587.43	629.05	655.81
Error [%]	4.48	2.28	6.64
Used RAM [MB]	481	1289	3517
Computing time [hh:mm:ss]	00:11:07	00:51:56	2:10:51

As a result of the calculation, it was found that the best agreement with the experiment is achieved at a particle distance of 2 mm (medium particle density). The same as in the previous paragraph, it results in a ratio between the projectile diameter and the particle distance of approximately 6:1. Note that simulation with the medium particle density and coarse mesh size (see Table 3.4) requires much less RAM and computing time than models with medium and fine mesh size (see Table 3.3)..

**3.2.2.3 Different FEM-to-SPH triggering criterion values**

One of the important parameters in this problem is the value of the adaptive FEM-SPH triggering criterion. An important feature is that this parameter is an artificial value and cannot be obtained from experiments. Since the perforation process leads to significant distortion of FE mesh in the impact area, a shear strain is defined as a triggering criterion. The triggering value of shear strain is varied in a wide range from 0.04 to 0.32 to evaluate its influence. Simulation results with a different value of triggering criterion, and different mesh sizes are presented in Figure 3.8 and Table 3.5.

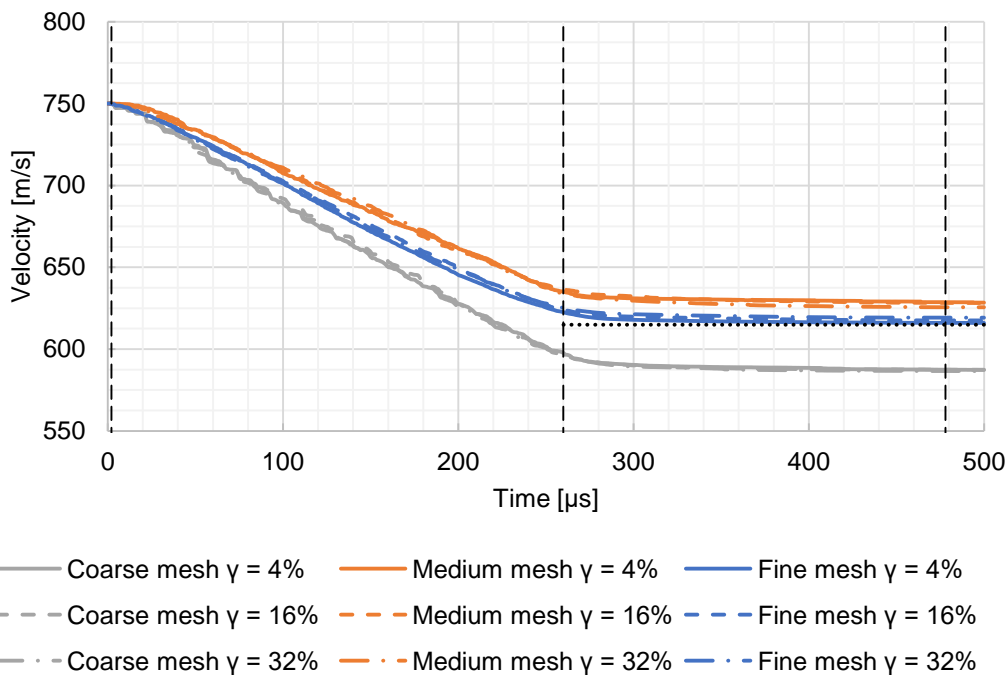


**Figure 3.8 – Projectile velocity corresponding to different triggering criterion value and mesh size**

**Table 3.5 – Simulation results and requested computational resources for different triggering criterion values**

	Mesh size								
	Coarse mesh			Medium mesh			Fine mesh		
Shear strain [-]	0.04	0.16	0.32	0.04	0.16	0.32	0.04	0.16	0.32
Residual velocity [m/s]	587.43	587.33	586.59	628.34	628.14	625.65	616.09	617.54	619.25
Error [%]	4.48	4.50	4.62	2.17	2.14	1.73	0.18	0.41	0.69

As it follows from Figure 3.8 and Table 3.5, the triggering criterion value almost does not affect the simulation results for any mesh size. It is explained by the fact that both the FEM and the SPH method lead to the correct results. The criterion of triggering from one method to another only determines the moment from which the calculation is carried out by the SPH method and thus does not affect simulation results. It is also established that triggering criterion value does not influence on computing time.

#### 4 Conclusion

1. Significant FEM mesh distortion leads to smaller time steps and longer computation time in explicit dynamic codes such as LS-DYNA. It may also give non-physical and wrong results. The SPH meshless method is able to give correct results in high-nonlinear dynamic problems that are consistent with the experiment. The coupled FEM-SPH method requires less computational resources than SPH, and it gives accurate results as well.

2. The CSCM concrete model with identified parameters gives identical results for different concrete grades both in FEM and SPH simulations and agrees with the Eurocode data well. The difference from the Eurocode data for the quasi-static cube compression problem does not exceed 7% in FEM and 3.8% in the SPH method, respectively.

3. It is recommended to use a computational model with spacing between FE nodes and between SPH particles in the range from 2 mm to 4 mm to obtain reasonable results in high-velocity ballistic problems. The difference from experiments decreases from 4.5% to 0.2% then the spacing decreases from 4 mm to 2 mm.

4. The best match is achieved at the spacing value of 2 mm. The ratio between the projectile diameter and the spatial discretization of approximately 6:1. This conclusion is consistent with the results of the aluminum plate perforation problem [24].

5. In this paper, shear strain is used as a triggering criterion from the FEM to the SPH method. The value of shear strain in the range from 0.04 to 0.32 is considered. As calculations show, the value of the triggering criterion does not influence on modeling results and computing time for any case of spatial discretization.

#### 5 References

1. Dmitriev, A., Novozhilov, Y., Mikhalyuk, D., Lalin, V. Calibration and Validation of the Menetrey-Willam Constitutive Model for Concrete; 2020; Construction of Unique Buildings and Structures. 2020. 88. Pp. 8804. DOI:10.18720/CUBS.88.4.
2. Belytschko, T., Liu, W., Moran, B. Nonlinear finite elements for continua and structures. Choice Reviews Online. 2001. 38(07). Pp. 38-3926-38-3926. DOI:10.5860/CHOICE.38-3926. URL: <http://choicereviews.org/review/10.5860/CHOICE.38-3926>.
3. Zienkiewicz, O., Taylor, R., Zhu, J.Z. The Finite Element Method: its Basis and Fundamentals. 7th ed. Elsevier Ltd, 2013. 714 p. ISBN:9781856176330.
4. Fries, T.P., Belytschko, T. The extended/generalized finite element method: An overview of the method and its applications. International Journal for Numerical Methods in Engineering. 2010. 84(3). Pp. 253-304. DOI:10.1002/nme.2914.
5. Lalin, V. V., Dmitriev, A.N., Diakov, S.F. Nonlinear deformation and stability of geometrically exact elastic arches. Magazine of Civil Engineering. 2019. 89(5). Pp. 39-51. DOI:10.18720/MCE.89.4.
6. Lalin, V. V., Yavarov, A. V., Orlova, E.S., Gulov, A.R. Application of the Finite Element Method for the Solution of Stability Problems of the Timoshenko Beam with Exact Shape Functions. Power Technology and Engineering. 2019. 53(4). Pp. 449-454. DOI:10.1007/s10749-019-01098-6.
7. Lalin, V., Nenashev, V., Utimisheva, I., Orlovich, R. Buckling of Cantilever Beam Loaded by Potential Following Moment. Lecture Notes in Civil Engineering. 70. Springer, 2020. Pp. 643-652.
8. Lalin, V.V., Kushova, D.A. New results in dynamics stability problems of elastic rods. Applied Mechanics and Materials. 2014. 617. Pp. 181-186. DOI:10.4028/www.scientific.net/AMM.617.181.
9. Lalin, V. V., Beliaev, M.O. Bending of geometrically nonlinear cantilever beam. Results obtained by Cosserat - Timoshenko and Kirchhoff's rod theories. Magazine of Civil Engineering. 2015. 53(1). DOI:10.5862/MCE.53.5.

10. Novozhilov, Y. V., Dmitriev, A.N., Mikhailuk, D.S., Chernukha, N.A., Feoktistova, L.Y., Volkodav, I.A. Aircraft NPP Impact Simulation Methodology. 16th International LS-DYNA® Users Conference. 2020. Pp. 1–14.
11. Novozhilov, Y.V., Mikhailuk, D.S., Feoktistova, L.Y. Calculation of aircraft impact load on the NPP nuclear island buildings. *Computational Continuum Mechanics*. 2018. 11(3). Pp. 288–301. DOI:10.7242/1999-6691/2018.11.3.22. URL: <http://journal.permsc.ru/index.php/ccm/article/view/CCMv11n3a22> (date of application: 21.09.2020).
12. Gertsik, S.M., Novozhilov, Y.V. NUMERICAL SIMULATION OF A MASSIVE IMPACTOR FALLING ONTO A REINFORCED CONCRETE BEAM. *Problems of Strength and Plasticity*. 2020. 82(1). Pp. 5–15. DOI:10.32326/1814-9146-2020-82-1-5-15. URL: <http://ppp.mech.unn.ru/index.php/ppp/article/view/553> (date of application: 21.09.2020).
13. Terranova, B., Whittaker, A., Schwer, L. Simulation of wind-borne missile impact using Lagrangian and Smooth Particle Hydrodynamics formulations. *International Journal of Impact Engineering*. 2018. 117. Pp. 1–12. DOI:10.1016/j.ijimpeng.2018.02.010.
14. Attaway, S.W., Heinstein, M.W., Swegle, J.W. Coupling of smooth particle hydrodynamics with the finite element method. *Nuclear Engineering and Design*. 1994. 150(2–3). Pp. 199–205. DOI:10.1016/0029-5493(94)90136-8. URL: <https://linkinghub.elsevier.com/retrieve/pii/0029549394901368> (date of application: 10.06.2020).
15. Wu, H., Peng, Y., Kong, X. Notes on projectile impact analyses. Singapore, Springer Nature, 2019. 1–370 p. ISBN:9789811332531.
16. Gingold, R.A., Monaghan, J.J. Kernel estimates as a basis for general particle methods in hydrodynamics. *Journal of Computational Physics*. 1982. 46(3). Pp. 429–453. DOI:10.1016/0021-9991(82)90025-0. URL: <https://linkinghub.elsevier.com/retrieve/pii/0021999182900250> (date of application: 10.06.2020).
17. Monaghan, J.J. Smoothed Particle Hydrodynamics. *Annual Review of Astronomy and Astrophysics*. 1992. 30(1). Pp. 543–574. DOI:10.1146/annurev.aa.30.090192.002551. URL: <http://www.annualreviews.org/doi/10.1146/annurev.aa.30.090192.002551> (date of application: 10.06.2020).
18. Gingold, R.A., Monaghan, J.J. Smoothed Particle Hydrodynamics: Theory and Application to Non-spherical Stars. *Monthly Notices of the Royal Astronomical Society*. 1977. 189. Pp. 375–389. DOI:10.16309/j.cnki.issn.1007-1776.2003.03.004.
19. Lucy, L.B. A numerical approach to the testing of the fission hypothesis. *The Astronomical Journal*. 1977. 82(12). Pp. 1013–1024. DOI:10.1007/s00769-003-0757-y. URL: <http://link.springer.com/10.1007/s00769-003-0757-y>.
20. Monaghan, J.J., Gingold, R.A. Shock simulation by the particle method SPH. *Journal of Computational Physics*. 1983. 52(2). Pp. 374–389. DOI:10.1016/0021-9991(83)90036-0.
21. Libersky, L.D., Petschek, A.G., Carney, T.C., Hipp, J.R., Allahdadi, F.A. High Strain Lagrangian Hydrodynamics. *Journal of Computational Physics*. 1993. 109(1). Pp. 67–75. DOI:10.1006/jcph.1993.1199. URL: <https://linkinghub.elsevier.com/retrieve/pii/S002199918371199X>.
22. Liu, G.R., Liu, M.B. Smoothed Particle Hydrodynamics: A Meshfree Particle Method. World Scientific Publishing Co. Pte Ltd, 2003. 449 p.
23. Li, S., Liu, W.K. Meshfree Particle Methods. Springer-Verlag Berlin Heidelberg, 2007. 508 p. ISBN:9783540222569.
24. Schwer, L.E. Aluminium plate perforation: a comparative case study using Lagrange with erosion, multi-material ALE, and smooth particle hydrodynamics. 7th European LS-DYNA Conference. 2009.
25. Zhang, Z., Qiang, H., Gao, W. Coupling of smoothed particle hydrodynamics and finite element method for impact dynamics simulation. *Engineering Structures*. 2011. 33. Pp. 255–264. DOI:10.1016/j.engstruct.2010.10.020. URL: [www.elsevier.com/locate/engstruct](http://www.elsevier.com/locate/engstruct) (date of application: 10.06.2020).
26. Fang, Q., Wu, H. Concrete Structures Under Projectile Impact. Singapore, Springer Singapore, 2017. 577 p. ISBN:978-981-10-3619-4.
27. Hanchak, S.J., Forrestal, M.J., Young, E.R., Ehrgott, J.Q. Perforation of concrete slabs with 48 MPa (7 ksi) and 140 MPa (20 ksi) unconfined compressive strengths. *International Journal of Impact Engineering*. 1992. 12(1). Pp. 1–7. DOI:10.1016/0734-743X(92)90282-X.

28. Hallquist, J. LS-DYNA theory manual. Livermore, Livermore Software Technology Corporation, 2007. 884 p. ISBN:9254492507.
29. De Vuyst, T., Vignjevic, R., Campbell, J.C. Coupling between meshless and finite element methods. *International Journal of Impact Engineering*. 2005. 31(8). Pp. 1054–1064. DOI:10.1016/j.ijimpeng.2004.04.017.
30. Wu, Y., Magallanes, J.M., Choi, H.-J., Crawford, J.E. Evolutionarily Coupled Finite-Element Mesh-Free Formulation for Modeling Concrete Behaviors under Blast and Impact Loadings. *Journal of Engineering Mechanics*. 2013. 139(4). Pp. 525–536. DOI:10.1061/(ASCE)EM.1943-7889.0000497. URL: <http://ascelibrary.org/doi/10.1061/%28ASCE%29EM.1943-7889.0000497> (date of application: 10.06.2020).
31. Wu, J., Wu, H., Tan, H.W.A., Chew, S.H. *Multi-layer Pavement System under Blast Load*. Singapore, Springer Singapore, 2018. 239 p. ISBN:978-981-10-5000-8.
32. Murray, Y. *Users Manual for LS-DYNA Concrete Material Model 159.* McLean, 2007. 77 p.
33. Murray, Y., Abu-Odeh, A., Bligh, R. *Evaluation of LS-DYNA Concrete Material Model 159.* McLean, 2007. 206 p.
34. Wei, J., Li, J., Wu, C. An experimental and numerical study of reinforced conventional concrete and ultra-high performance concrete columns under lateral impact loads. 2019. DOI:10.1016/j.engstruct.2019.109822. URL: <https://doi.org/10.1016/j.engstruct.2019.109822> (date of application: 26.07.2020).
35. Weng, Y.-H., Qian, K., Fu, F., Fang, Q. Numerical investigation on load redistribution capacity of flat slab substructures to resist progressive collapse. *Journal of Building Engineering*. 2020. 29. Pp. 101109. DOI:10.1016/j.job.2019.101109. URL: <https://doi.org/10.1016/j.job.2019.101109> (date of application: 26.07.2020).
36. Saini, D., Shafei, B. Concrete constitutive models for low velocity impact simulations. 2019. DOI:10.1016/j.ijimpeng.2019.103329. URL: <https://doi.org/10.1016/j.ijimpeng.2019.103329> (date of application: 26.07.2020).
37. Levi-Hevroni, D., Kochavi, E., Kofman, B., Gruntman, S., Sadot, O. Experimental and numerical investigation on the dynamic increase factor of tensile strength in concrete. 2017. DOI:10.1016/j.ijimpeng.2017.12.006. URL: <https://doi.org/10.1016/j.ijimpeng.2017.12.006> (date of application: 26.07.2020).
38. Jiang, H., Zhao, J. Calibration of the continuous surface cap model for concrete. 2015. DOI:10.1016/j.finel.2014.12.002. URL: <http://dx.doi.org/10.1016/j.finel.2014.12.002> (date of application: 26.07.2020).
39. EN1992-1-1. *Eurocode 2: Design of concrete structures - Part 1-1: General rules and rules for buildings*. European Committee for Standardization, 2004. 227 p.
40. EN 12390-3:2009 *Testing Hardened Concrete. - Part 3: Compressive Strength of Test Specimens*. European Committee for Standardization, 2009. 22 p.

## ANNEX A

\*MAT\_CSCM parameters for different concrete grades

Unit system: ton-mm-s-N-MPa

## Concrete C20

*MAT_CSCM_TITLE								
C20								
\$#	mid	ro	nplot	incre	irate	erode	recov	itretrc
	1	2.4E-9	1	0.0	1	0.99	10.0	0
\$#	pred							
	0.0							
\$#	g	k	alpha	theta	lamda	beta	nh	ch
	12630.0	16840.0	4.748	0.3454	1.295	0.1029	0.0	0.0
\$#	alpha1	thetal	lamda1	beta1	alpha2	theta2	lamda2	beta2
	0.8332	0.0	0.2559	0.0169	0.7646	0.0	0.2646	0.0169
\$#	r	xd	w	d1	d2			
	2.68	51.14	0.0656	1.1000E-42	2.22500E-6			
\$#	b	gfc	d	gft	gfs	pwr	pwrt	pmo
	100.0	6.41	0.1	0.0641	0.0641	5.0	1.0	0.0
\$#	eta0c	nc	etaot	nt	overc	overt	srate	rep0w
	1.19900E-4	0.785	4.7000E-5	0.48	18.83	18.83	1.0	1.0

## Concrete C30

*MAT_CSCM_TITLE								
C30								
\$#	mid	ro	nplot	incre	irate	erode	recov	itretrc
	2	2.4E-9	1	0.0	1	0.99	10.0	0
\$#	pred							
	0.0							
\$#	g	k	alpha	theta	lamda	beta	nh	ch
	13980.0	18640.0	7.72	0.3399	3.06	0.05301	0.0	0.0
\$#	alpha1	thetal	lamda1	beta1	alpha2	theta2	lamda2	beta2
	0.82	0.0	0.2407	0.01132	0.76	0.0	0.26	0.01132
\$#	r	xd	w	d1	d2			
	2.283	73.85	0.0656	1.1000E-42	2.22500E-6			
\$#	b	gfc	d	gft	gfs	pwr	pwrt	pmo
	100.0	7.938	0.1	0.07938	0.07938	5.0	1.0	0.0
\$#	eta0c	nc	etaot	nt	overc	overt	srate	rep0w
	1.00300E-4	0.786	1.7600E-5	0.48	21.45	21.45	1.0	1.0

## Concrete C40

*MAT_CSCM_TITLE								
C40								
\$#	mid	ro	nplot	incre	irate	erode	recov	itretrc
	3	2.4E-9	1	0.0	1	0.99	10.0	0
\$#	pred							
	0.0							
\$#	g	k	alpha	theta	lamda	beta	nh	ch
	15110.0	20150.0	11.1	0.3339	5.271	0.03235	0.0	0.0
\$#	alpha1	thetal	lamda1	beta1	alpha2	theta2	lamda2	beta2
	0.82	0.0	0.2407	0.008618	0.76	0.0	0.26	0.008618
\$#	r	xd	w	d1	d2			
	2.092	92.77	0.0656	1.1000E-42	2.22500E-6			
\$#	b	gfc	d	gft	gfs	pwr	pwrt	pmo
	100.0	9.348	0.1	0.09348	0.09348	5.0	1.0	0.0
\$#	eta0c	nc	etaot	nt	overc	overt	srate	rep0w
	1.34500E-4	0.787	2.2100E-5	0.48	26.69	26.69	1.0	1.0

## Concrete C50

*MAT_CSCM_TITLE								
C50								
\$#	mid	ro	nplot	incre	irate	erode	recov	itretrc
	4	2.4E-9	1	0.0	1	0.99	10.0	0
\$#	pred							
	0.0							
\$#	g	k	alpha	theta	lamda	beta	nh	ch
	16100.0	21460.0	15.0	0.3271	8.111	0.02206	0.0	0.0
\$#	alpha1	theta1	lamda1	beta1	alpha2	theta2	lamda2	beta2
	0.82	0.0	0.2407	0.006974	0.76	0.0	0.26	0.006974
\$#	r	xd	w	d1	d2			
	2.012	111.7	0.0656	1.1000E-42	2.22500E-6			
\$#	b	gfc	d	gft	gfs	pwrc	pwrt	pmod
	100.0	10.67	0.1	0.1067	0.1067	5.0	1.0	0.0
\$#	eta0c	nc	etaot	nt	overc	overt	srate	rep0w
	2.22300E-4	0.788	6.0600E-5	0.48	34.55	34.55	1.0	1.0